



# Ethanol oxidation reaction (EOR) investigation on Pt/C, Rh/C, and Pt-based bi- and tri-metallic electrocatalysts: A DEMS and *in situ* FTIR study

Antoine Bach Delpuech<sup>a,b,c,\*</sup>, Frédéric Maillard<sup>b,c</sup>, Marian Chatenet<sup>b,c,1</sup>, Priscillia Soudant<sup>b,c</sup>, Carsten Cremers<sup>a</sup>

<sup>a</sup> Fraunhofer Institut für Chemische Technologie ICT, Joseph-von-Fraunhofer-Straße 7, 776327 Pfinztal, Germany

<sup>b</sup> Univ. Grenoble Alpes, LEPMI, F-38000 Grenoble, France

<sup>c</sup> CNRS, LEPMI, F-38000 Grenoble, France

## ARTICLE INFO

### Article history:

Received 14 June 2015

Received in revised form 20 August 2015

Accepted 24 August 2015

Available online 28 August 2015

### Keywords:

EOR

C–C bond cleavage

FTIR

DEMS

Electrocatalysis

## ABSTRACT

The ethanol oxidation reaction (EOR) was studied on Pt/C, Rh/C, Pt-Rh/C, Pt-SnO<sub>2</sub>/C and Pt-Rh-SnO<sub>2</sub>/C using on-line differential electrochemical mass spectrometry (DEMS) in a flow-cell system and *in situ* Fourier transform infrared spectroscopy (*in situ* FTIR). The electrocatalysts were synthesized by a modified polyol method and physically characterized by inductively-coupled plasma atomic emission spectroscopy (ICP-AES), X-ray diffraction (XRD) and transmission electron microscopy (TEM). The electrocatalytic activity of the materials was tested for the EOR and the electrooxidation of a monolayer of adsorbed CO (CO<sub>ad</sub> being an intermediate of the EOR). Both *in situ* FTIR and DEMS investigations revealed that CO<sub>ad</sub> electrooxidation occurs at lower potentials on Pt-SnO<sub>2</sub>/C and Pt-Rh-SnO<sub>2</sub>/C than on Pt/C, Rh/C and Pt-Rh/C. A good correspondence was found between the (intensity vs. potential) variations of the *m/z* = 22 mass-to-charge signal and of the IR band at 2343 cm<sup>-1</sup>, both strictly assigned to CO<sub>2</sub>. The addition of Rh to Pt enhances the tolerance to adsorbed CO molecules during the EOR (CO<sub>2</sub> molecules were detected at more negative potentials in FTIR on Rh-containing electrocatalysts), and the simultaneous presence of Pt, Rh and SnO<sub>2</sub> in the catalysts resulted in enhanced EOR selectivity towards CO<sub>2</sub>. The CO<sub>2</sub> current efficiency (CCE) calculations indicate quantitatively that the tri-metallic Pt-Rh-SnO<sub>2</sub>/C electrocatalyst yields more complete ethanol electrooxidation into CO<sub>2</sub>. Finally, FTIR experiments enabled to detect high-potential (*E* > 0.95 V vs. RHE) CO<sub>2</sub> formation, which likely originates from the oxidation of either CH<sub>x</sub>- or ethoxy-adsorbates that only oxidize at high potential.

© 2015 Elsevier B.V. All rights reserved.

## 1. Introduction

Research on small organic species has attracted growing attention over the last decades, due to the higher energy density of direct alcohol fuel cells (DAFC) compared to hydrogen-fed proton exchange membrane fuel cells (PEMFC). The ethanol non-toxicity, ease of storage and transport, as well as its possible production from biomass fermentation, makes it a promising candidate as DAFC fuel. Nonetheless, using ethanol creates multiple challenges, such as the difficulty to split the ethanol C–C bond and the sluggish ethanol

electrooxidation kinetics. As a result of its incomplete oxidation, the ethanol oxidation reaction (EOR) operates through different pathways, leading to the formation of acetaldehyde (2e<sup>-</sup>), and acetic acid (4e<sup>-</sup>) instead of carbon dioxide (CO<sub>2</sub>–12e<sup>-</sup> per ethanol molecule).

The EOR mechanism and kinetics have been extensively studied on bulk Pt [1–8] and Pt/C [9–12]. The specific activity towards the EOR reaches a maximum for carbon-supported Pt (Pt/C) nanoparticles ca. 2–3 nm in size [9]. CO<sub>2</sub> current efficiency (CCE) calculations conducted by means of differential electrochemical mass spectrometry (DEMS) on the same material revealed that between 5 and 20% of the overall EOR current (depending on the operating conditions) was generating CO<sub>2</sub> [13–16]. Besides the detection of the acetic acid, acetaldehyde and CO<sub>2</sub> as final products of the EOR, *in situ* Fourier transform infrared (*in situ* FTIR) spectroscopy mea-

\* Corresponding author.

E-mail address: [antoine.bachdelpuech@gmail.com](mailto:antoine.bachdelpuech@gmail.com) (A. Bach Delpuech).

<sup>1</sup> Member of the French University Institute (IUF), Paris, France.

<sup>2</sup> Present address: Department of Chemical Sciences, University of Padova, Via Marzolo 1, (PD), Padova, I-35131, Italy.

surements indicate that CO, acetaldehyde and acetate are reaction intermediates on Pt [1,2,17–19].

During the past few years, the research on bi- and tri-metallic electrocatalysts has intensified in order to improve the EOR selectivity toward CO<sub>2</sub> generation [12,13,20–27]. So far, Pt-SnO<sub>2</sub>/C electrocatalysts have demonstrated the highest EOR specific activity [12,28]. The addition of SnO<sub>2</sub> to Pt leads to a negative shift of the onset potential of the EOR and improves its selectivity toward acetic acid formation [20,28]. This enhanced electroactivity is accounted for by a bi-functional mechanism between Pt and SnO<sub>2</sub> moieties [29], in which the oxophilic character of Sn enables the formation of OH<sub>ad</sub>-species from water dissociation at lower potential, these species favoring the further oxidation of adsorbed acetaldehyde into acetic acid. However, the EOR selectivity toward CO<sub>2</sub> production is not improved on Pt-SnO<sub>2</sub>/C in comparison to Pt/C. On the contrary, owing to the capability of Rh to cleave the ethanol C–C bond [30], a higher EOR selectivity toward CO<sub>2</sub> generation has been demonstrated on Pt-Rh/C [13,15,16]. Besides, the EOR onset is also negatively shifted on Pt-Rh/C against Pt/C: this phenomenon is explained by the easier dehydrogenation taking place on Pt-Rh/C [23]. Interestingly, recent studies on Pt-Rh-SnO<sub>2</sub>/C have shown encouraging EOR performances [25,31–33]. A lower EOR overpotential and a larger EOR activity have been recorded on the tri-metallic electrocatalyst compared to Pt/C and Pt-Rh/C [25,32].

In the present study, the EOR has been investigated on Pt/C, Rh/C, Pt-Rh/C, Pt-SnO<sub>2</sub>/C and Pt-Rh-SnO<sub>2</sub>/C by means of on-line DEMS and *in situ* FTIR spectroscopy. The electrocatalysts were physically characterized by thermogravimetric analysis (TGA) and inductively-coupled plasma atomic emission spectroscopy (ICP-AES), powder X-ray diffraction (XRD) and transmission electron microscopy (TEM) to determine the metal-to-carbon ratio, the size of the metal crystallites/nanoparticles and their distribution on the carbon support. A DEMS study was carried out using the  $m/z=22$ ,  $m/z=29$  and  $m/z=61$  mass-to-charge signals, which are representative for CO<sub>2</sub>, acetaldehyde and ethyl acetate formation, respectively. The latter, product of the esterification of acetic acid with ethanol, is an indirect proof of the formation of acetic acid during the electrochemical reactions [34]. The CO<sub>2</sub> current efficiency (CCE) of the EOR was determined after calibration of the  $m/z=22$  signal. The *in situ* FTIR study compares qualitatively the relative distribution of the products on each electrocatalyst.

## 2. Experimental

### 2.1. Materials preparation

Carbon-supported Pt/C, Rh/C, Pt-Rh/C, Pt-SnO<sub>2</sub>/C, Pt-Rh-SnO<sub>2</sub>/C, with 20 wt.% overall metal load, were prepared using a modified polyol method. In a typical procedure, the calculated amount of metal precursors, H<sub>2</sub>PtCl<sub>6</sub> (Aldrich), RhCl<sub>3</sub>·xH<sub>2</sub>O (Aldrich) and SnCl<sub>2</sub>, was dissolved in a solution containing water and ethylene glycol (EG) (volume ratio 2:1), prior to the addition of carbon black (Vulcan XC-72R, Cabot) dispersed in an EG solution by sonication. The pH of the solution was subsequently adjusted to 12 using a 0.5 M NaOH solution (diluted in EG). The solution was stirred for one hour at ambient temperature, thereafter heated up to  $T=433$  K, maintained at this temperature for three hours and cooled down overnight. The pH of the solution was then fixed to 3 using a 0.5 M H<sub>2</sub>SO<sub>4</sub> solution and stirred for 24 h. Finally, the electrocatalyst powder was filtered, washed copiously with distilled water and dried overnight in an oven at  $T=353$  K.

### 2.2. Physico-chemical characterizations

The metal ratio in the electrocatalysts was verified by thermogravimetric analysis (TGA, Q 5000 from TA Instruments). The composition of the bi- and tri-metallic electrocatalysts was mea-

sured by ICP-AES (iCAP 6300 Thermo). The crystalline structure and the average crystallite size of the metal nanoparticles was determined by powder X-ray diffraction (XRD, Bruker AXS D8) in the  $2\theta$  range from 15° to 90° using Cu K $\alpha$  radiation with a scan rate of 0.74° min<sup>-1</sup>. Representative transmission electron microscopy (TEM, Jeol 2010) micrographs were used to reconstruct the nanoparticle size distribution (PSD) histograms (ca. 400 nanoparticles being counted for the construction of each PSD histogram).

### 2.3. Electrochemical measurements

In DEMS experiments, a suspension composed of 5 wt.% Nafion® solution (Aldrich), 3 mg of electrocatalyst, and 400  $\mu$ L of an isopropanol:water solution (volume ratio 3:1) was ultrasonically treated for 10 min to obtain a well-dispersed ink. Thin-film working electrodes (87.5  $\mu$ g cm<sup>-2</sup>) were then prepared by depositing 12  $\mu$ L of this suspension onto a thin, porous gold layer (1 cm<sup>2</sup> area), obtained by Au sputtering onto a Gore-Tex PTFE membrane (60  $\mu$ m thickness, 0.02  $\mu$ m mean pore size, 50% porosity). 5 wt.% Nafion®, used as ionomer, was further deposited to stabilize the catalytic particles on the electrode surface, and accounted for 50 wt.% of the total dry mass. The counter-electrode was a platinum foil and the reference electrode a freshly-prepared reversible hydrogen electrode (RHE); all potential values are expressed on the RHE scale. The DEMS experiments were carried out in a flow-cell system described elsewhere [35]. A GAMRY Reference 3000 potentiostat connected to a Balzers QMS 200 mass spectrometer was used to control the potential of the working electrode. The CO<sub>ad</sub>-stripping experiments were carried out in 0.5 M H<sub>2</sub>SO<sub>4</sub> supporting electrolyte, while the EOR was investigated in 0.5 M H<sub>2</sub>SO<sub>4</sub> + 0.1 M EtOH.

The *in situ* FTIR experiments were performed using a Bruker Vertex 70 V spectrometer equipped with a mercury cadmium telluride (MCT) detector cooled with liquid nitrogen. Each FTIR spectrum was obtained under p-polarization and acquired during 30 s as an average of 256 interferograms. The reflectance spectra were recorded every 100 mV from  $E=0.25$  to 1.15 V vs. RHE and are represented hereafter as  $R/R_{\text{Ref}}$ , with  $R_{\text{Ref}}$  the reflectance spectrum recorded at  $E_{\text{ref}}=0.15$  V vs. RHE. The spectral resolution was 4 cm<sup>-1</sup>. A three-electrode setup was employed to run the electrochemical measurements. The counter electrode was a Pt grid and the reference electrode a RHE. The working electrode was either an Au electrode (for the CO<sub>ad</sub>-stripping study) or a GC electrode (for the EOR study) on which was deposited a uniform ink of the prepared electrocatalyst (from 5 to 30  $\mu$ L, depending on the electrocatalyst). The ink was prepared with 2 mg electrocatalyst dispersed by sonication in a mixture of 18  $\mu$ L 5% Nafion® solution, 8  $\mu$ L isopropanol and 1.3 mL milli-Q water. In order to minimize the infrared beam absorption by the aqueous solution, the working electrode was pressed by a glass rod against the CaF<sub>2</sub> optical window used for the *in situ* FTIR experiments, therefore allowing working in a thin layer configuration.

Prior to the *in situ* FTIR measurements, five voltammograms between  $E=0.05$  and 1.2 V vs. RHE were recorded in a 0.5 M H<sub>2</sub>SO<sub>4</sub> solution to obtain the characteristic voltammetric response of the electrocatalysts. Afterward, a proper amount of ethanol was introduced in the electrochemical cell so as to obtain a 0.5 M H<sub>2</sub>SO<sub>4</sub> + 1.0 M EtOH electrolyte solution. The addition of ethanol was accomplished under fixed potential at  $E=0.05$  V vs. RHE to hamper ethanol adsorption on the electrocatalyst surface. Ethanol adsorption in the H<sub>upd</sub> region is indeed hindered by the presence of hydrogen adsorbates [36,37]. Finally, still under fixed potential, the solution was let under Ar bubbling during 5 min to homogenize the solution before positioning the working electrode against the optical window. The electrochemical experiments were run with an Autolab PGSTAT 302N potentiostat.

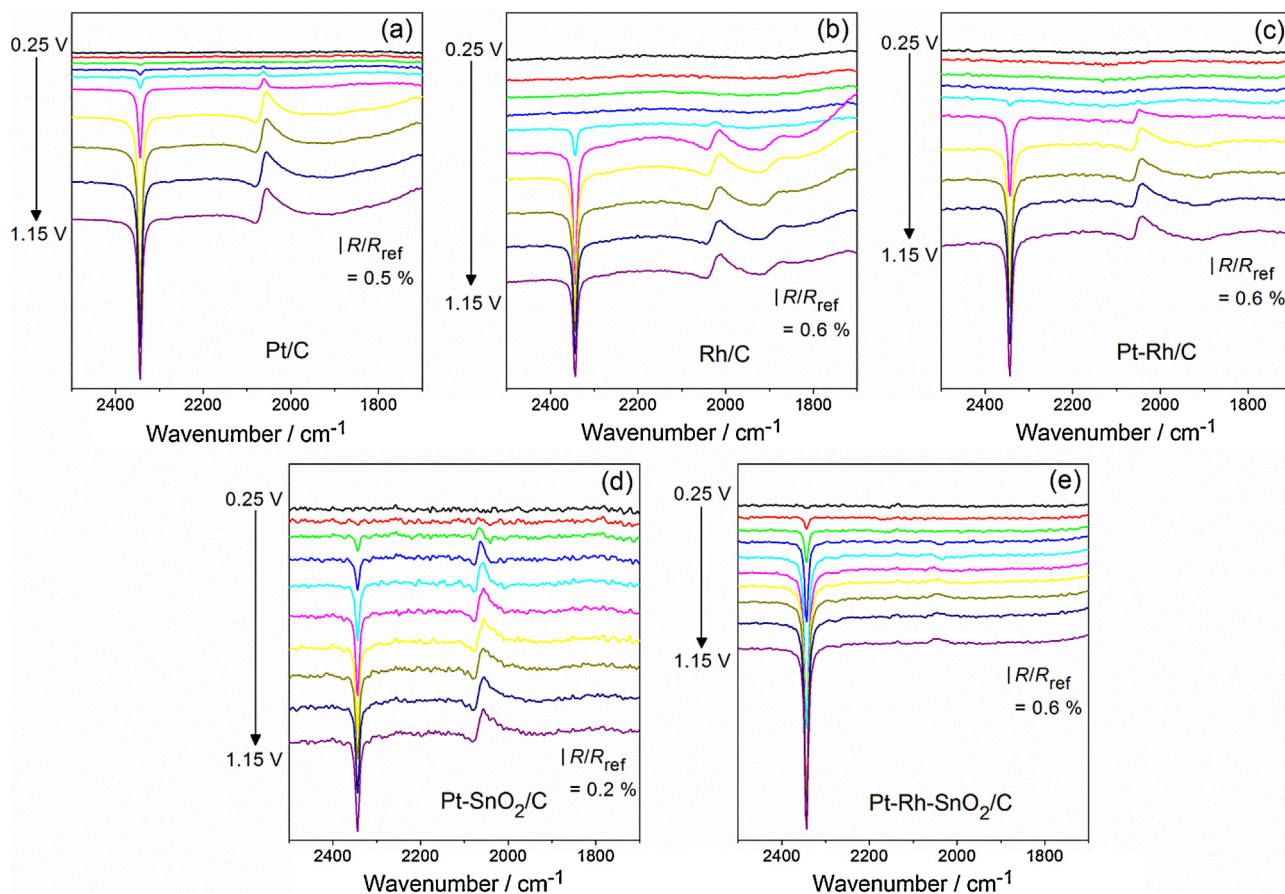


Fig. 1. In-situ infrared spectra recorded upon  $\text{CO}_{\text{ad}}$ -stripping in 0.5 M  $\text{H}_2\text{SO}_4$  on (a) Pt/C, (b) Rh/C, (c) Pt-Rh/C, (d) Pt-SnO<sub>2</sub>/C and (e) Pt-Rh-SnO<sub>2</sub>/C;  $T = 298 \text{ K}$ .

**Table 1**  
Structural proprieties of Pt/C, Rh/C, Pt-Rh/C, Pt-SnO<sub>2</sub>/C and Pt-Rh-SnO<sub>2</sub>/C

Electrocatalyst	Effective composition by ICP-AES	$a/\text{\AA}$	$d_{\text{XRD}}/\text{nm}$	$d_{\text{Elec}}/\text{nm}$	$d_{\text{N}}/\text{nm}$	$d_{\text{S}}/\text{nm}$	$d_{\text{V}}/\text{nm}$
Pt/C	–	3.93	5.8	4.8	2.3	2.6	2.9
Rh/C	–	3.84	2.8	3.8	2.1	2.4	2.7
Pt-Rh/C	Pt <sub>1</sub> Rh <sub>0.8</sub> /C	3.91	3.5	4.2	2.3	3.3	3.9
Pt-SnO <sub>2</sub> /C	Pt <sub>1</sub> (SnO <sub>2</sub> ) <sub>0.3</sub> /C	3.97	4.5	9.4	3.3	5.8	7.8
Pt-Rh-SnO <sub>2</sub> /C	Pt <sub>1</sub> Rh <sub>0.58</sub> (SnO <sub>2</sub> ) <sub>0.35</sub> /C	3.91	3.4	4.8	2.4	2.6	2.8

$a$ , lattice parameter;  $d_{\text{XRD}}$ , mean nanoparticle size (XRD);  $d_{\text{Elec}}$ , electrochemical mean particle size;  $d_{\text{N}}$ , number-averaged diameter (TEM);  $d_{\text{S}}$ , surface-averaged diameter (TEM);  $d_{\text{V}}$ , volume-averaged diameter (TEM).

For the sake of comparison, all electrochemical results presented hereafter are normalized by the metal mass at the working electrode.

#### 2.4. Calibration of the mass spectrometer

The calibration of the  $m/z = 22$  mass-to-charge signal is necessary to quantify the part of current originating from the total electrooxidation of ethanol into  $\text{CO}_2$ , as detected by DEMS [38]. To do so,  $\text{CO}_{\text{ad}}$ -stripping is used as reference electrochemical reaction, since the number of electrons exchanged per  $\text{CO}_2$  molecule is well known (two electrons per  $\text{CO}_2$  molecule):



The  $m/z = 22$  signal is the only MS signal which is solely attributed to the production of  $\text{CO}_2$  during ethanol electrooxidation (doubly ionized  $[\text{CO}_2^{++}]$ ). Indeed, the  $m/z = 44$  signal, also used in the literature to quantify  $\text{CO}_2$  (ionized  $[\text{CO}_2^+]$ ) [15,39–41], can be compromised by acetaldehyde (ionized  $[\text{CH}_3\text{CHO}^+]$ ), a known by-product of the EOR.

The ionic current for the  $m/z = 22$  signal and the faradaic current are correlated by Eq. (2):

$$K_{22}^* = \frac{2 I_{m/z=22, \text{CO}}}{I_{f, \text{CO}}} \quad (2)$$

where  $I_{m/z=22, \text{CO}}$  is the ionic charge of  $m/z = 22$  mass-to-charge signal,  $I_{f, \text{CO}}$  the faradaic charge, 2 the number of electrons exchanged during the electrooxidation of adsorbed CO in  $\text{CO}_2$  and  $K_{22}^*$  the calibration constant of the  $m/z = 22$  signal.

The  $\text{CO}_2$  current efficiency (CCE) was deduced using the faradaic and ionic current values obtained during the ethanol electrooxidation:

$$\text{CCE} = \frac{6}{K_{22}^*} \frac{I_{m/z=22}}{I_f} \quad (3)$$

with 6 the average number of electrons exchanged per produced  $\text{CO}_2$  molecule.



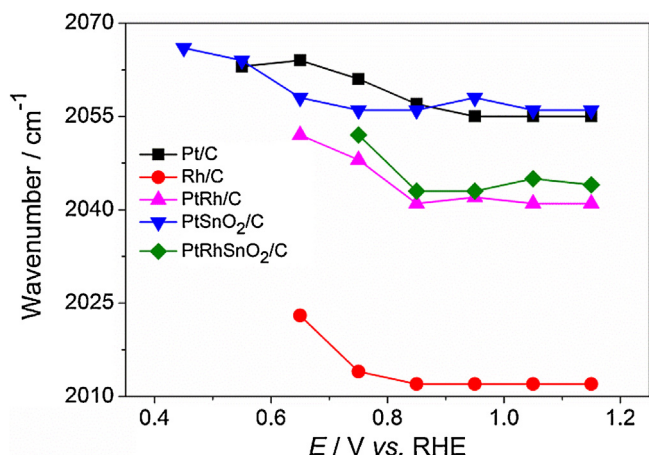


**Fig. 2.** Variation of the CO<sub>L</sub> band wavenumber versus potential, measured during the CO<sub>ad</sub>-stripping in 0.5 M H<sub>2</sub>SO<sub>4</sub> on Pt/C, Rh/C, Pt-Rh/C, Pt-SnO<sub>2</sub>/C and Pt-Rh-SnO<sub>2</sub>/C;  $T = 298$  K.

### 3. Results and discussion

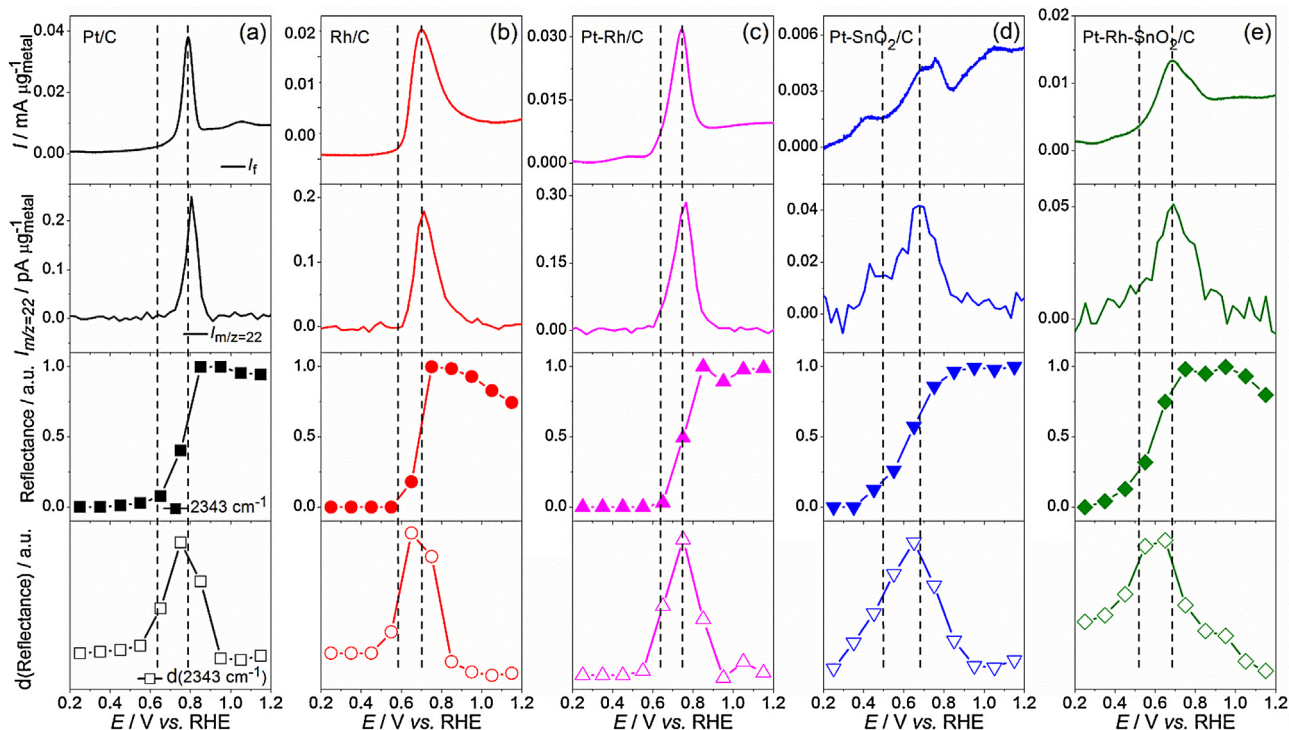
#### 3.1. Physical characterization

The physical characterization of the home-made Pt/C, Rh/C, Pt-Rh/C, Pt-SnO<sub>2</sub>/C and Pt-Rh-SnO<sub>2</sub>/C electrocatalysts synthesized by the polyol method is thoroughly detailed in [42]. The chemical and morphological information of the electrocatalysts was obtained by TGA, ICP-AES, XRD and TEM and is summarized in Table 1. To summarize, all electrocatalysts crystallized in a face-centered cubic (fcc) structure, as demonstrated by XRD. Their mean particle size  $d_{\text{XRD}}$  was determined using Scherrer's law on the (200) diffraction peak. The TEM images revealed the presence of well dispersed nanoparticles on the carbon support with a narrow size distribution. Associated particle size distribution (PSD) histograms enabled

the determination of the nanoparticles number- ( $d_N$ ), surface- ( $d_S$ ) and volume-averaged ( $d_V$ ) diameters.  $d_N$  is rather similar for all electrocatalysts (ca.  $d_N = 2.2$  nm), except for Pt-SnO<sub>2</sub>/C (ca. 3.3 nm) which presents large nanoparticles and agglomerates on the carbon surface.  $d_S$  can be compared to  $d_{\text{Elec}}$ , which was calculated with the knowledge of the electrochemically active surface area (ECSA) determined by CO stripping. Their comparison shows some discrepancies which is attributed for the multi-metallic electrocatalysts to an underestimation of the ECSA (and thus overestimation of  $d_{\text{Elec}}$ ) due to the CO<sub>ad</sub> electrooxidation already taking place during the potentiostatic step prior to the stripping-CV. The comparison between  $d_V$  and  $d_{\text{XRD}}$  shows a good agreement between the values for the electrocatalysts, except for Pt/C and Pt-SnO<sub>2</sub>/C, which is likely due to the presence of agglomerates in both samples.

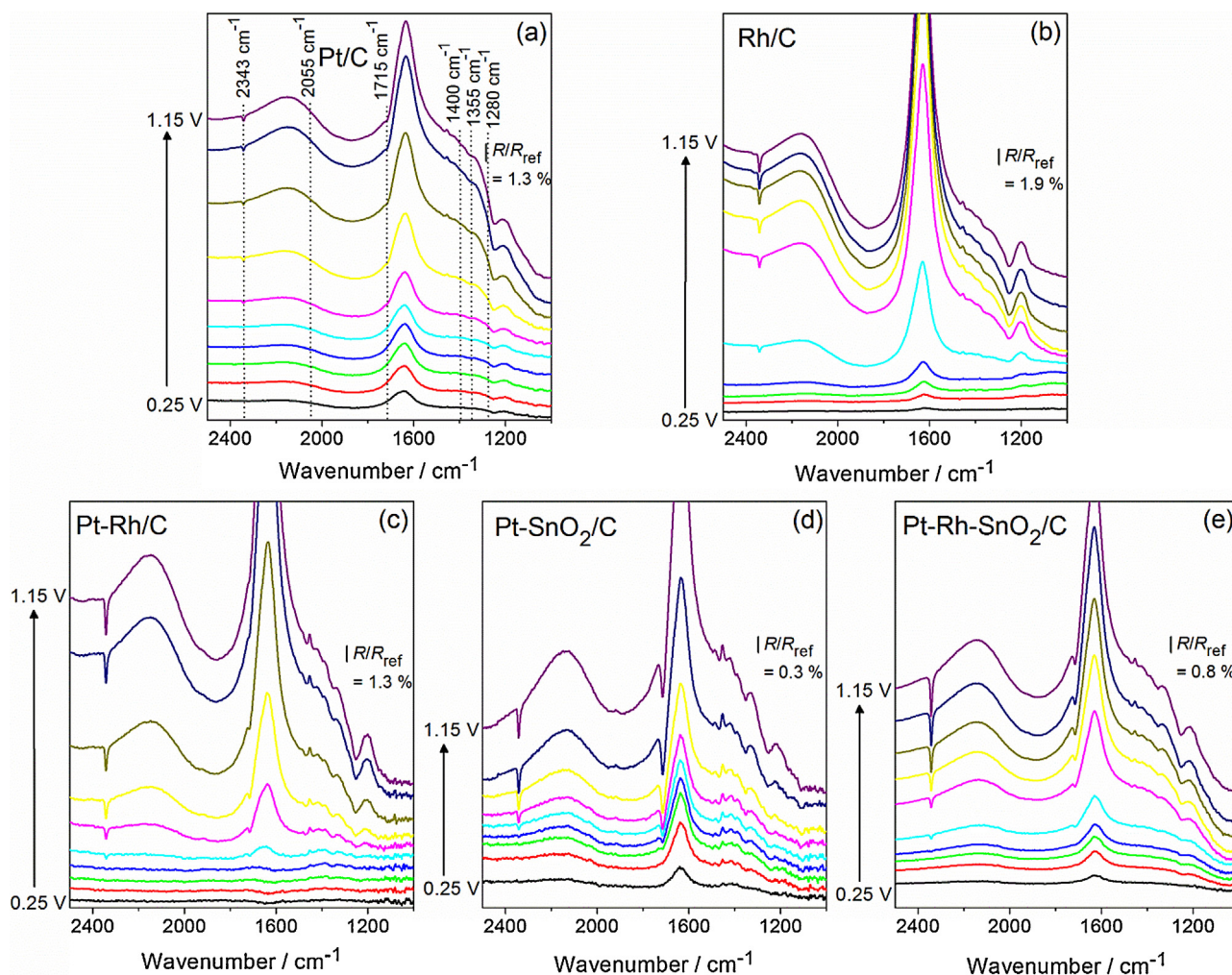
#### 3.2. CO stripping

Fig. 1 shows typical FTIR spectra recorded during the electrooxidation of a CO<sub>ad</sub> monolayer on Pt/C, Rh/C, Pt-Rh/C, Pt-SnO<sub>2</sub>/C and Pt-Rh-SnO<sub>2</sub>/C. The spectra were recorded between  $E = 0.25$  and 1.15 V vs. RHE and compared to a reference spectrum taken at  $E_{\text{ref}} = 0.15$  V vs. RHE. The bands located at ca. 2055 cm<sup>-1</sup> and 1820–1840 cm<sup>-1</sup> are ascribed to linearly-bonded CO<sub>L</sub> (C–O) and bridge-bonded CO<sub>B</sub> (C=O), respectively [1,43–46]. The band at 2343 cm<sup>-1</sup> is attributed to the O–C–O asymmetric stretching mode [47]. Its appearance in the FTIR spectra is indicative of the onset of the CO<sub>ad</sub> electrooxidation reaction. As it can be seen in Fig. 1, the adsorption of CO molecules in bridge configuration is hardly visible on Pt/C (its presence can be guessed at  $E = 0.85$  and 0.95 V vs. RHE, the band being centered at 1830 cm<sup>-1</sup>). A favored on-top CO adsorption on Pt/C could rationalize this quasi-absence of a band between 1820 and 1840 cm<sup>-1</sup> [48]. An additional explanation could be that water H–O–H bending mode [49] overlaps with the CO<sub>B</sub> band. On the contrary, CO<sub>L</sub> and CO<sub>B</sub> bands are clearly observed on Rh/C, despite the overlapping with the H–O–H bending mode of water at ca. 1645 cm<sup>-1</sup>. Qualitatively, the ratio between on-top



**Fig. 3.** (Top) CO<sub>ad</sub>-stripping voltammogram in 0.5 M H<sub>2</sub>SO<sub>4</sub> and (middle top) corresponding  $m/z = 22$  mass-to-charge signal, (middle bottom) CO<sub>2</sub> band intensity and (bottom) its derivative on (a) Pt/C, (b) Rh/C, (c) Pt-Rh/C, (d) Pt-SnO<sub>2</sub>/C and (e) Pt-Rh-SnO<sub>2</sub>/C;  $v = 10$  mV s<sup>-1</sup>;  $T = 298$  K.





**Fig. 4.** In situ infrared spectra recorded in 0.5 M  $\text{H}_2\text{SO}_4$  + 0.1 M EtOH on (a) Pt/C, (b) Rh/C, (c) Pt-Rh/C, (d) Pt-SnO<sub>2</sub>/C and (e) Pt-Rh-SnO<sub>2</sub>/C at room temperature;  $R_{\text{ref}} = 0.15$  V vs. RHE. Potential range:  $E = 0.25$  and  $1.15$  V vs. RHE; Potential step:  $E = 0.1$  V.

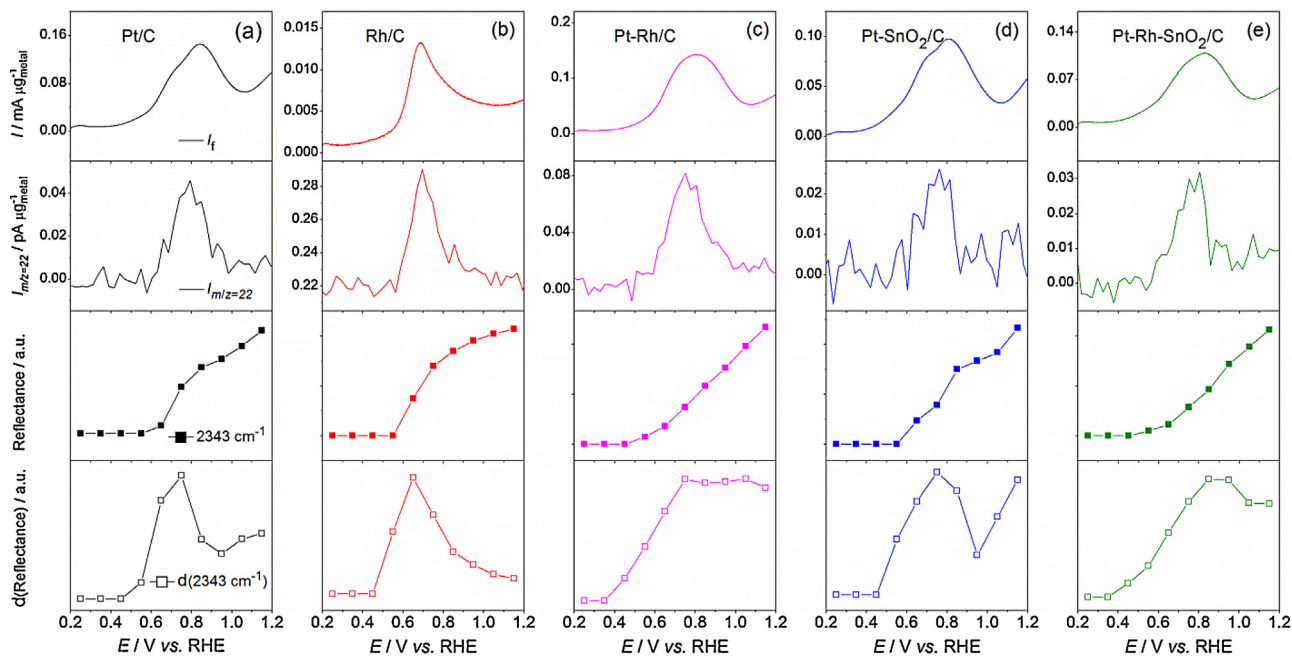


**Fig. 5.** (Top) EOR cyclic voltammogram (in 0.5 M  $\text{H}_2\text{SO}_4$  + 0.1 M EtOH) and (middle top) corresponding MSCV  $m/z=22$  compared to (middle bottom)  $\text{CO}_2$  infrared band ( $2343 \text{ cm}^{-1}$ ) and (bottom) its derivative on (a) Pt/C, (b) Rh/C, (c) Pt-Rh/C, (d) Pt-SnO<sub>2</sub>/C and (e) Pt-Rh-SnO<sub>2</sub>/C;  $v = 10 \text{ mV s}^{-1}$ ;  $T = 298 \text{ K}$ .

and two-fold bridge  $\text{CO}_{\text{ad}}$  is more balanced than on Pt/C. On Pt-Rh/C and Pt-SnO<sub>2</sub>/C, the  $\text{CO}_{\text{B}}$  band appears broader, and tails until 1750–1700  $\text{cm}^{-1}$ . It is worthwhile noting that the intensity of the  $\text{CO}_{\text{L}}$  band was lower on Pt-Rh-SnO<sub>2</sub>/C compared to the other electrocatalysts: this may be indicative of a lower  $\text{CO}_{\text{ad}}$  coverage on Pt-Rh-SnO<sub>2</sub>/C (50 at.% Pt) compared to the other electrocatalysts. Similar conclusions were recently achieved by Silva-Junior et al. on Pt-Rh-SnO<sub>2</sub>/C (relative to Pt-Rh/C) [50].

Similar to what was found for Ru/C and Pt-Ru/C electrocatalysts [51,52], the  $\text{CO}_{\text{L}}$  band is red shifted (i.e. shifted to lower wavenumbers) on Rh/C compared to Pt/C (2015  $\text{cm}^{-1}$  vs. 2055  $\text{cm}^{-1}$ , respectively). This may indicate a stronger CO adsorption on the Rh/C surface in comparison to Pt/C. The  $\text{CO}_{\text{L}}$  band was also red shifted on Pt-Rh/C (at 2041  $\text{cm}^{-1}$ ) and Pt-Rh-SnO<sub>2</sub>/C (at 2046  $\text{cm}^{-1}$ ) relative to Pt/C, but a similar position was noticed for Pt-SnO<sub>2</sub>/C (2056  $\text{cm}^{-1}$ ). These results suggest that Rh modifies to some extent the electronic structure of Pt (note however that the formation of a Pt-Rh alloy is thermodynamically unfavorable at the temperature at which the Pt-Rh/C electrocatalyst was synthesized) [53] contrary to SnO<sub>2</sub>.

It is generally possible to distinguish IR bands of adsorbed species from solution species by observing the shift of the IR bands position against the electrode potential. This shift can be rationalized by two phenomena [54]: the influence of the electrode potential on the adsorbates, also commonly referred to as the Stark effect [55,56]; the effect of the adsorbates distribution on the electrode surface with increasing potential, altering the adsorbates vibrations frequency, also called the dipole–dipole coupling effect [54,57], or changing the chemical bond between the adsorbates and the electrocatalyst, known as the chemical shift effect [58]. Fig. 2 illustrates the changes of the  $\text{CO}_{\text{L}}$  band wavenumber as a function of the electrode potential for the synthesized electrocatalysts. As a pure Stark effect would have translated by a shift toward positive wavenumbers with increasing electrode potentials, the observed red-shift indicates that dipole–dipole coupling variations are dominating the spectra. The decrease of the dipole–dipole coupling reflects the decrease of the  $\text{CO}_{\text{ad}}$ -coverage, and thus the weaker lateral interactions between the CO-adsorbates, with increasing electrode potentials [59–61].

Fig. 3 compares the *in situ* FTIR and the on-line DEMS results obtained on the synthesized electrocatalysts. To that goal, (i) the  $\text{CO}_{\text{ad}}$ -stripping current, (ii) the  $m/z = 22$  mass-to-charge signal were compared to (iii) the intensity of the  $\text{CO}_2$  band at 2343  $\text{cm}^{-1}$  plotted vs. the electrode potential (normalized by the obtained highest band) and to (iv) its associated derivative. As it can be seen in Fig. 3, the use of the derivative (Fig. 3, bottom) enables to correct the effect of accumulation of reaction products in the thin layer in the *in situ* FTIR experimental condition and to get an excellent agreement between the  $\text{CO}_{\text{ad}}$ -stripping measurements performed in the very different DEMS and *in situ* FTIR experimental conditions. Thus this technique can be used for more complex reactions like the EOR.

For all the electrocatalysts, the onset potential of the  $\text{CO}_{\text{ad}}$ -stripping experiment (symbolized by the dashed line at low potential—Fig. 3, top), matches remarkably well with that monitored by DEMS (Fig. 3, middle top), and by *in situ* FTIR (Fig. 3, middle bottom and bottom). The  $\text{CO}_{\text{ad}}$ -stripping onset potential is negatively shifted on Pt-SnO<sub>2</sub>/C ( $E = 0.37$  V vs. RHE) and Pt-Rh-SnO<sub>2</sub>/C ( $E = 0.35$  V vs. RHE) compared to Pt/C ( $E = 0.64$  V vs. RHE). The  $\text{CO}_{\text{ad}}$  electrooxidation is also favored on Rh/C, but no striking difference appears between Pt/C and Pt-Rh/C. The more facile  $\text{CO}_{\text{ad}}$  electrooxidation on Pt-SnO<sub>2</sub>/C and Pt-Rh-SnO<sub>2</sub>/C is ascribed to the oxophilic character of SnO<sub>2</sub>, which supplies OH-species at low potentials on the electrocatalyst surface, thereby facilitating the oxidation of the

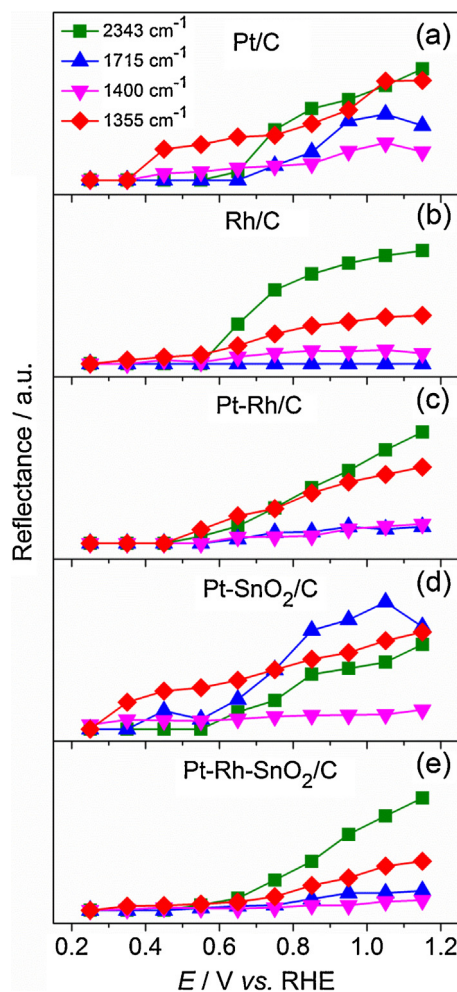


Fig. 6. Change of the IR band intensities (at 2343, 1715, 1400, 1355  $\text{cm}^{-1}$ ) vs. the electrode potential on (a) Pt/C (b) Rh/C, (c) Pt-Rh/C, (d) Pt-SnO<sub>2</sub>/C and (e) Pt-Rh-SnO<sub>2</sub>/C.

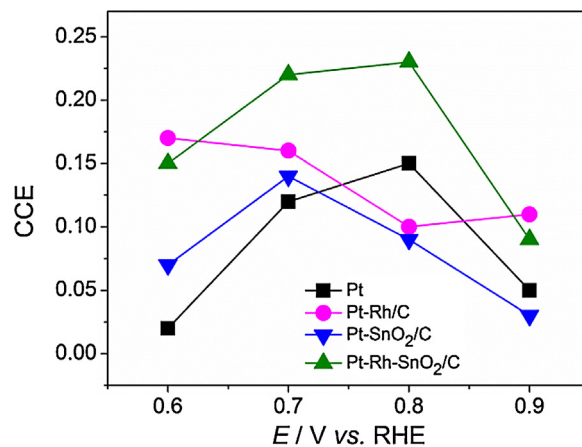


Fig. 7. (a) EOR  $\text{CO}_2$  current efficiency (CCE) values calculated from cyclic voltammograms run in 0.5 M  $\text{H}_2\text{SO}_4$  + 0.1 M EtOH and corresponding MSCVs (represented in Fig. 6) on Pt/C, Pt-Rh/C, Pt-SnO<sub>2</sub>/C and Pt-Rh-SnO<sub>2</sub>/C. Reproduced from [42] with permission from the PCCP Owner Societies.



**Table 2**  
Band assignment for the EOR products.

Wavenumber (cm <sup>-1</sup> )	Species	References
2343	O–C–O asymmetric stretching	[47]
2055	C–O stretching	[1,43–46]
1715	C=O stretching from –COOH or –CHO	[47,74]
1400	C–O symmetric stretching of adsorbed CH <sub>3</sub> COO <sup>-</sup>	[17,74,75]
1355	CH <sub>3</sub> symmetric deformation	[17,76]
1280	OH deformation + C–O stretching from –COOH	[17,74]
1120	C–H wagging vibration	[17,76]

CO<sub>ad</sub> molecules adsorbed on Pt and Rh (bi-functional mechanism, often mentioned for CO and methanol oxidation reactions) [62].

### 3.3. Ethanol oxidation reaction

#### 3.3.1. EOR on Pt- and Rh-based electrocatalysts by in situ FTIR

Fig. 4 shows FTIR reflectance spectra acquired during successive potential steps (100 mV each) between  $E = 0.25$  and  $1.15$  V vs. RHE in  $0.5$  M H<sub>2</sub>SO<sub>4</sub> +  $1$  M EtOH on Pt/C, Rh/C, Pt-Rh/C, Pt-SnO<sub>2</sub>/C and Pt-Rh-SnO<sub>2</sub>/C electrocatalysts. Down-pointing (negative) bands indicate the production of species in the thin layer contained between the working electrode and the CaF<sub>2</sub> prism, while up-pointing (positive) bands represent the consumption/depletion of other species. Note that, due to the non-negligible electrocatalytic activity of Au towards the EOR, a glassy carbon was used as substrate for the electrocatalyst [63].

The positive band located at  $1640$  cm<sup>-1</sup>, assigned to the water H–O–H bending mode [49], dominates all the IR spectra. The broad positive band at ca.  $1200$  cm<sup>-1</sup> is attributed to the doubly degenerated stretch mode of bisulfate anions, in agreement with previous findings on mono- and polycrystalline electrodes [55,64–69]. Other positive bands at  $1454$  cm<sup>-1</sup> and  $1085$  cm<sup>-1</sup> indicate that ethanol is depleted from the thin layer as the electrode potential is increased. This variation goes along with that of two other bands detected at  $2908$  cm<sup>-1</sup> and  $2983$  cm<sup>-1</sup> (not shown here), which are ascribed to ethanol asymmetric CH<sub>2</sub> and CH<sub>3</sub> vibrations, respectively [19]. Finally, a broad positive band centered at ca.  $1915$  cm<sup>-1</sup> appears in Fig. 4 in the medium potential region ( $0.5 < E < 1.15$  V vs. RHE) on all studied electrocatalysts. This band is similar to that monitored at  $1920$  cm<sup>-1</sup> on Pt(100), which was ascribed to asymmetric bridge-bonded CO<sub>B</sub> [43] despite the nearly  $50$  cm<sup>-1</sup> wavenumber difference with values reported in the literature [70]. This band is also visible in other *in situ* FTIR EOR studies [5,50,71–73], but was not discussed in these studies.

Negative-going bands may also be observed in Fig. 4. The bands at  $2055$  cm<sup>-1</sup> and  $2343$  cm<sup>-1</sup> are ascribed to linearly bonded CO<sub>L</sub> and CO<sub>2</sub> formation, respectively [1,43–46]. The signal of the first band was however small in our experimental conditions. The bands observed at  $1280$  cm<sup>-1</sup>,  $1400$  cm<sup>-1</sup> and  $1715$  cm<sup>-1</sup> are characteristic of aqueous acetic acid formation [17,74]. They are ascribed to the coupled O–H deformation [17] and C–O stretching from –COOH [17,74], to C–O symmetric stretching of adsorbed CH<sub>3</sub>COO<sup>-</sup> [17,74,75] and C=O stretching mode from –COOH or –CHO [47,74], respectively. Acetaldehyde characteristic bands may be found at  $1355$  cm<sup>-1</sup> (double band –CH<sub>3</sub> symmetric deformation) [17,76],  $1120$  cm<sup>-1</sup> (C–H wagging vibration) [17,76] and  $1715$  cm<sup>-1</sup> (stretching mode of carbonyl groups) [47]. A summary of the bands positions and their assignment is given in Table 2.

#### 3.3.2. Comparing in situ FTIR and on-line DEMS measurements.

Fig. 5 compares the evolution of the faraday current and of the associated  $m/z = 22$  signal with that of CO<sub>2</sub> IR band and of its derivative against the potential for Pt/C, Rh/C, Pt-Rh/C, Pt-SnO<sub>2</sub>/C and Pt-Rh-SnO<sub>2</sub>/C. Similarly to what was observed for the CO<sub>ad</sub>-stripping experiment, the derivative of the CO<sub>2</sub> band evolution

correlates fairly well with the ionic current, both of them having the same shape (at least until ca.  $E = 0.9$  V vs. RHE) and reaching a maximum at ca.  $0.75 < E < 0.8$  V vs. RHE. In addition, not only the CO<sub>2</sub> IR band continues increasing in contrast to the potentiodynamic current, but its derivative, either remains constant (on Pt-Rh/C and Pt-Rh-SnO<sub>2</sub>/C) or, after a first decrease between  $E = 0.75$  and  $0.95$  V vs. RHE, increases again at ca.  $E > 0.95$  V vs. RHE (on Pt/C and Pt-SnO<sub>2</sub>/C), contrary to what was observed for the CO<sub>ad</sub>-stripping experiments (Fig. 3). For this reason, this rise cannot be only imputed to an accumulation effect and must be rather associated with the production of CO<sub>2</sub> during a chemical/electrochemical reaction. Although this hypothesis is difficult to prove/contradict if one considers the low signal-to-noise ratio of the  $m/z = 22$  signals, the higher baseline at  $0.95 < E < 1.2$  V vs. RHE compared to that at  $0.2 < E < 0.55$  V vs. RHE may be ascribed to the formation of CO<sub>2</sub>. The degradation of the carbon support could also lead to the formation of CO<sub>2</sub>, but is believed not to significantly account for the increase in the baseline in the potential region  $0.95$  V vs. RHE  $< E < 1.2$  V vs. RHE [77]. Indeed, such degradation would have been observed by mass spectrometry or infrared spectroscopy during the CO<sub>ad</sub>-stripping study, but neither a change of the baseline (for the  $m/z = 22$  signal) nor an increase of the derivative of the CO<sub>2</sub> IR band were detected in this experiment (see Fig. 3). For this reason, the rise of the CO<sub>2</sub> band derivative is preferentially attributed to the electrooxidation of strong ethanol adsorbates oxidizing only at high electrode potential, as also pointed out in the literature [13]. Note also that acetaldehyde, produced during ethanol electrooxidation and trapped inside the thin layer cavity, may also further react and oxidize into CO<sub>2</sub>.

For Rh/C (Fig. 5b), the derivative of the CO<sub>2</sub> IR band and the  $m/z = 22$  signal have a similar profile over the whole studied potential range. Contrary to what is observed for Pt/C (Fig. 5a), the derivative steadily decreases at  $E > 0.65$  V vs. RHE, which shows that no CO<sub>2</sub> is formed at high potential on Rh/C. On the opposite, the derivative of the CO<sub>2</sub> band has a similar trend on Pt-based multimetallic electrocatalysts and on Pt/C: it remains either constant (for Pt-Rh/C and Pt-Rh-SnO<sub>2</sub>/C—Fig. 5b and d respectively) or increases (for Pt-SnO<sub>2</sub>/C—Fig. 5c) at ca.  $E > 0.95$  V vs. RHE. This demonstrates that there is a steady formation of CO<sub>2</sub> at high potential, which most likely originates from the electrochemical ethanol electrooxidation reaction. This is confirmed by the baseline of the  $m/z = 22$  signal which, particularly in the case of Pt-Rh/C and Pt-Rh-SnO<sub>2</sub>/C, is higher at  $0.95 < E < 1.2$  V vs. RHE than at  $0.2 < E < 0.55$  V vs. RHE. This formation of CO<sub>2</sub> is tentatively explained by the electrooxidation of strong ethanol adsorbates, i.e. CH<sub>x</sub>- [3,30,36,78,80–84] or/and ethoxy-adsorbates [3,36], which are formed before the complete coverage of the electrocatalyst surface by oxygenated species from the water dissociation. Their oxidation should be distinguished from the CO<sub>2</sub> production in medium potential range originating directly from the oxidation of CO<sub>ad</sub> (issued from ethanol dissociative adsorption). The ethoxy-adsorbates are assumed to oxidize solely at ca.  $E > 0.9$  V vs. RHE to form CO<sub>2</sub> (or reduce at low potential and produce methane or ethane) [36,37], while CH<sub>x,ad</sub> were also found to oxidize at  $E > 0.9$  V vs. RHE [36,37], although their oxidation was also reported to oxidize at ca.  $E > 0.4$  V vs. RHE [4,79]. The absence of CO<sub>2</sub> formation on Rh/C at high potential undeniably proves that the CO<sub>2</sub> molecules generated on Pt-based electrocatalysts in this potential region do not originate from a degradation of the carbon support, but are produced by the electrooxidation of ethanol.

Fig. 6 shows the evolution of the IR bands at  $2343$  cm<sup>-1</sup>,  $1915$  cm<sup>-1</sup>,  $1715$  cm<sup>-1</sup>,  $1400$  cm<sup>-1</sup> and  $1355$  cm<sup>-1</sup> as a function of the electrode potential on Pt/C, Rh/C, Pt-Rh/C, Pt-SnO<sub>2</sub>/C and Pt-Rh-SnO<sub>2</sub>/C. Note that the graph indicates at which potential the EOR products are generated, but does not allow any quantitative evaluation. One firstly sees that CO<sub>2</sub> is generated at lower potential

( $E=0.55$  V vs. RHE) on Pt-Rh/C and Pt-Rh-SnO<sub>2</sub>/C than on the other electrocatalysts ( $E=0.65$  V vs. RHE). These results differ from what was observed during the CO<sub>ad</sub>-stripping experiments, where Pt-SnO<sub>2</sub>/C and Pt-Rh-SnO<sub>2</sub>/C displayed the lowest CO<sub>ad</sub> electrooxidation onset potential values. This confirms previous literature findings [24,30,85] demonstrating that rhodium eases the C–C bond cleavage, therefore favoring complete electrooxidation of ethanol in this potential region compared to Pt/C or Pt-SnO<sub>2</sub>/C. Providing OH-species at low potentials, as does Pt-SnO<sub>2</sub>/C, is required to oxidize the CO<sub>ad</sub>-species formed from ethanol dissociative adsorption, but not sufficient to selectively produce CO<sub>2</sub>.

When comparing the different bands with one another, it can be noticed that, for the same quantity of metal deposited onto the glassy carbon substrate, Pt-Rh-SnO<sub>2</sub>/C displays the highest CO<sub>2</sub> band intensity relatively to the other bands ascribed to acetaldehyde and acetic acid, followed by Rh/C and Pt-Rh/C. These results semi-quantitatively suggest that CO<sub>2</sub> formation is best favored on Pt-Rh-SnO<sub>2</sub>/C, among the family of Rh-based electrocatalysts. While Rh helps to cleave the C–C bond, SnO<sub>2</sub> provides OH-species at low potential and frees Rh (and Pt) atoms from the hydroxide adsorbates. Fig. 6 also undeniably shows that the addition of SnO<sub>2</sub> to Pt does not improve the electrocatalyst ability to break the C–C bond. On the contrary, the large intensity of the bands at 1715 cm<sup>−1</sup> and 1355 cm<sup>−1</sup> suggest that acetaldehyde formation is favored on the Pt-SnO<sub>2</sub>/C. This result is in contradiction with previous studies [72,86,87], which indicated that acetic acid formation is favored on Pt-SnO<sub>2</sub>/C. Conversely, CO<sub>2</sub> formation is slightly promoted on Pt-Rh/C versus Pt/C, alike the DEMS results reported in the previous section and in the literature [13,15].

The CO<sub>2</sub> current efficiency (CCE) vs. the electrode potential is displayed in Fig. 7. The CCE values were determined from potentiodynamic voltammetries and the corresponding  $m/z=22$  signal between  $E=0.5$  and  $0.9$  V vs. RHE ( $0.1$  V step) on Pt/C, Pt-Rh/C, Pt-SnO<sub>2</sub>/C and Pt-Rh-SnO<sub>2</sub>/C according to the procedure detailed in the experimental section.

The CCE evolution can be separated in two regions for all electrocatalysts: a first ascending phase between  $E=0.5$  and ca.  $0.7$ – $0.8$  V vs. RHE, where the CCE increases with the electrode potential; a second one at  $E>0.7$ – $0.8$  V vs. RHE, where the CCE decreases when the potential increases. The CCE rise in the first potential region is likely due to the increasing coverage in OH<sub>ad</sub>, which triggers the oxidation of adsorbed CO into CO<sub>2</sub>. In the second potential region ( $E>0.7$ – $0.8$  V vs. RHE), the decrease of the CO<sub>2</sub> generation is tentatively explained by the poisoning of the catalytic surface with OH<sub>ad</sub> species coming from water dissociation and ethanol adsorbates [3,78], which prevents ethanol dissociative adsorption and a fortiori CO<sub>2</sub> generation. More details about those phenomena are given in [42].

Among the studied electrocatalysts, Pt-Rh-SnO<sub>2</sub>/C demonstrates the highest CCE on the whole potential range, while Pt/C and Pt-SnO<sub>2</sub>/C displays the lowest values in the potential range  $E=0.6$ – $0.7$  V vs. RHE. Fig. 7 confirms quantitatively the qualitative comparison done in Fig. 6, which evidenced by *in situ* FTIR that the complete EOR was favored on Pt-Rh-SnO<sub>2</sub>/C.

#### 4. Conclusions

A comparative study of the EOR was carried out on Pt/C, Rh/C, Pt-Rh/C, Pt-SnO<sub>2</sub>/C and Pt-Rh-SnO<sub>2</sub>/C electrocatalysts by means of *in situ* Fourier transform infrared spectroscopy (*in situ* FTIR) and differential electrochemical mass spectrometry (DEMS). The study focused mainly on the promotion of the EOR complete pathway, leading to CO<sub>2</sub>, versus partial ones forming acetaldehyde and acetic acid as final products, for the different Pt-based electrocatalysts.

The electrooxidation of CO initiates at lower potentials on Pt-SnO<sub>2</sub>/C and Pt-Rh-SnO<sub>2</sub>/C compared to Pt/C, Rh/C and Pt-Rh/C, as indicated by *in situ* FTIR and DEMS measurements. No further shift could however be noticed on Pt-Rh-SnO<sub>2</sub>/C compared to Pt-SnO<sub>2</sub>/C. Despite the different experimental conditions, a good correlation between the *in situ* FTIR and DEMS results was demonstrated.

According to both techniques, CO<sub>2</sub> production during the EOR initiates at slightly lower potential on Rh-based electrocatalysts compared to Pt/C. Besides, the *in situ* FTIR measurements qualitatively featured enhanced CO<sub>2</sub> production on Pt-Rh-SnO<sub>2</sub>/C, comparatively to acetaldehyde and acetic acid formation. This result is confirmed and quantified via CCE calculations from the DEMS measurements, which indicate larger CO<sub>2</sub> formation on the tri-metallic electrocatalyst compared to the other ones. The use of the derivative of the CO<sub>2</sub> IR band enabled the detection of CO<sub>2</sub> at high potential ( $E>0.95$  V vs. RHE), which could however not be confirmed with certainty by the present DEMS results on Pt-based electrocatalysts. This formation of CO<sub>2</sub> is thought to originate from the oxidation of either CH<sub>x</sub>- or ethoxy-adsorbates.

#### Acknowledgements

Financial support of his work by the German Federal Ministry of Research (BMBF) and the French National Research Agency (ANR) through the “Program Inter Carnot Fraunhofer” part project “Efficient use of Bio-Ethanol in Fuel Cells (EUBECCELL)” is gratefully acknowledged. This work was partly performed within the framework of the Centre of Excellence of Multifunctional Architected Materials “CEMAM” no. AN-10-LABX-44-01. M. Chatenet thanks the Institut Universitaire de France (IUF) for its support.

#### References

- [1] L.-W.H. Leung, M.J. Weaver, J. Electroanal. Chem. Interfacial Electrochem. 240 (1988) 341–348.
- [2] L.-W.H. Leung, S.-C. Chang, M.J. Weaver, J. Electroanal. Chem. Interfacial Electrochem. 266 (1989) 317–336.
- [3] T. Iwasita, E. Pastor, Electrochim. Acta 39 (1994) 531–537.
- [4] S.C.S. Lai, M.T.M. Koper, Faraday Discuss. 140 (2009) 399.
- [5] G.A. Camara, T. Iwasita, J. Electroanal. Chem. 578 (2005) 315–321.
- [6] M.J. Giz, G.A. Camara, J. Electroanal. Chem. 625 (2009) 117–122.
- [7] D. Bayer, S. Berenger, M. Joos, C. Cremers, J. Tübke, Int. J. Hydrogen Energy 35 (2010) 12660–12667.
- [8] D. Bayer, S. Berenger, C. Cremers, J. Tübke, ECS Trans. 25 (2010) 95–103.
- [9] J. Perez, V.A. Paganin, E. Antolini, J. Electroanal. Chem. 654 (2011) 108–115.
- [10] V. Rao, C. Cremers, U. Stimming, L. Cao, S. Sun, S. Yan, et al., J. Electrochem. Soc. 154 (2007) B1138–B1147.
- [11] H. Wang, Z. Jusys, R.J. Behm, J. Phys. Chem. B. 108 (2004) 19413–19424.
- [12] H. Wang, Z. Jusys, R.J. Behm, J. Power Sources 154 (2006) 351–359.
- [13] A.B. Delpuech, T. Asset, M. Chatenet, C. Cremers, J. Electrochem. Soc. 161 (2014) F918–F924.
- [14] D.A. Cantane, W.F. Ambrosio, M. Chatenet, F.H.B. Lima, J. Electroanal. Chem. 681 (2012) 56–65.
- [15] F.H.B. Lima, D. Profeti, W.H. Lizcano-Valbuena, E.A. Ticianelli, E.R. Gonzalez, J. Electroanal. Chem. 617 (2008) 121–129.
- [16] K. Bergamaski, E.R. Gonzalez, F.C. Nart, Electrochim. Acta 53 (2008) 4396–4406.
- [17] T. Iwasita, B. Rasch, E. Cattaneo, W. Vielstich, Electrochim. Acta 34 (1989) 1073–1079.
- [18] X.H. Xia, H.-D. Liess, T. Iwasita, J. Electroanal. Chem. 437 (1997) 233–240.
- [19] J.M. Perez, B. Beden, F. Hahn, A. Aldaz, C. Lamy, J. Electroanal. Chem. Interfacial Electrochem. 262 (1989) 251–261.
- [20] L. Jiang, L. Colmenares, Z. Jusys, G.Q. Sun, R.J. Behm, Electrochim. Acta 53 (2007) 377–389.
- [21] F.H.B. Lima, E.R. Gonzalez, Electrochim. Acta 53 (2008) 2963–2971.
- [22] S. Sen Gupta, J. Datta, J. Electroanal. Chem. 594 (2006) 65–72.
- [23] K. Bergamaski, J.F. Gomes, B.E. Goi, F.C. Nart, Eclética Quím. 28 (2003) 87–92.
- [24] J.P.I. de Souza, S.L. Queiroz, K. Bergamaski, E.R. Gonzalez, F.C. Nart, J. Phys. Chem. B 106 (2002) 9825–9830.
- [25] A. Kowal, M. Li, M. Shao, K. Sasaki, M.B. Vukmirovic, J. Zhang, et al., Nat. Mater. 8 (2009) 325–330.
- [26] L.S. Parreira, J.C.M. da Silva, M. D’Vila-Silva, F.C. Simões, S. Garcia, I. Gaubeur, et al., Electrochim. Acta 96 (2013) 243–252.
- [27] G. García, N. Tsiouvaras, E. Pastor, M.A. Peña, J.L.G. Fierro, M.V. Martínez-Huerta, Int. J. Hydrogen Energy 37 (2012) 7131–7140.



- [28] C. Lamy, S. Rousseau, E.M. Belgsir, C. Coutanceau, J.-M. Léger, *Electrochim. Acta* 49 (2004) 3901–3908.
- [29] A.V. Tripković, K.D. Popović, J.D. Lović, V.M. Jovanović, S.I. Stevanović, D.V. Tripković, et al., *Electrochem. Commun.* 11 (2009) 1030–1033.
- [30] E. Méndez, J.L. Rodríguez, M.C. Arévalo, E. Pastor, *Langmuir* 18 (2002) 763–772.
- [31] M. Li, A. Kowal, K. Sasaki, N. Marinkovic, D. Su, E. Korach, et al., *Electrochim. Acta* 55 (2010) 4331–4338.
- [32] M. Li, W.-P. Zhou, N.S. Marinkovic, K. Sasaki, R.R. Adzic, *Electrochim. Acta* 104 (2013) 454–461.
- [33] L.C. Silva-Junior, G. Maia, R.R. Passos, E.A. de Souza, G.A. Camara, M.J. Giz, *Electrochim. Acta* 112 (2013) 612–619.
- [34] J. Wang, S. Wasmus, R.F. Savinell, *J. Electrochem. Soc.* 142 (1995) 4218–4224.
- [35] C. Cremers, D. Bayer, B. Kintzel, M. Joos, F. Jung, M. Krausa, et al., *ECS Trans.* 16 (2008) 1263–1273.
- [36] H. Wang, Z. Jusys, R.J. Behm, *Fuel Cells* 4 (2004) 113–125.
- [37] A. Bach Delpuech, M. Chatenet, C. Cremers, T. Tübke, *Electrochim. Acta* 141 (2014) 102–112.
- [38] H. Baltruschat, *J. Am. Soc. Mass Spectrom.* 15 (2004) 1693–1706.
- [39] J. Gomes, D. Profeti, L.J. Deiner, *ChemElectroChem* 1 (2014) 655–662.
- [40] A.A. Abd-El-Latif, E. Mostafa, S. Huxter, G. Attard, H. Baltruschat, *Electrochim. Acta* 55 (2010) 7951–7960.
- [41] M. Chojak Halseid, Z. Jusys, R.J. Behm, *J. Electroanal. Chem.* 644 (2010) 103–109.
- [42] A.B. Delpuech, M. Chatenet, M.S. Rau, C. Cremers, *Phys. Chem. Chem. Phys.* 17 (2015) 10881–10893.
- [43] S. Watanabe, J. Inukai, M. Ito, *Surf. Sci.* 293 (1993) 1–9.
- [44] F. Kitamura, M. Takeda, M. Takahashi, M. Ito, *Chem. Phys. Lett.* 142 (1987) 318–322.
- [45] F. Kitamura, M. Takahashi, M. Ito, *Surf. Sci.* 223 (1989) 493–508.
- [46] Y. Kinomoto, S. Watanabe, M. Takahashi, M. Ito, *Surf. Sci.* 242 (1991) 538–543.
- [47] G. Socrates, *Infrared and Raman Characteristic Group Frequencies: Tables and Charts*, John Wiley & Sons, 2004.
- [48] F. Maillard, S. Pronkin, E.R. Savinova, Size effects in electrocatalysis of fuel cell reactions on supported metal nanoparticles, in: T.M. Koper (Ed.), *Fuel Cell Catal.*, John Wiley & Sons, Inc., 2009, 2015, pp. 507–566.
- [49] T. Uchida, M. Osawa, J. Lipkowsky, *J. Electroanal. Chem.* 716 (2014) 112–119.
- [50] L.C. Silva-Junior, G. Maia, R.R. Passos, E.A. de Souza, G.A. Camara, M.J. Giz, *Electrochim. Acta* 112 (2013) 612–619.
- [51] F. Maillard, A. Bonnefont, M. Chatenet, L. Guétaz, B. Doisneau-Cottignies, H. Roussel, et al., *Electrochim. Acta* 53 (2007) 811–822.
- [52] F. Maillard, G.-Q. Lu, A. Wieckowski, U. Stimming, *J. Phys. Chem. B* 109 (2005) 16230–16243.
- [53] T.B. Massalski, H. Okamoto, *ASM International, Binary Alloy Phase Diagrams*, ASM International, Materials Park, Ohio, 1990.
- [54] T. Iwasita, F.C. Nart, *Prog. Surf. Sci.* 55 (1997) 271–340.
- [55] F.C. Nart, T. Iwasita, *J. Electroanal. Chem.* 322 (1992) 289–300.
- [56] A. Rodes, E. Pastor, T. Iwasita, *J. Electroanal. Chem.* 376 (1994) 109–118.
- [57] S.-C. Chang, M.J. Weaver, *J. Chem. Phys.* 92 (1990) 4582–4594.
- [58] F.M. Hoffmann, *Surf. Sci. Rep.* 3 (1983) 107–192.
- [59] S. Watanabe, J. Inukai, M. Ito, *Surf. Sci.* 293 (1993) 1–9.
- [60] S.C. Chang, L.-W.H. Leung, M.J. Weaver, *J. Phys. Chem.* 93 (1989) 5341–5345.
- [61] M. Arenz, K.J.J. Mayrhofer, V. Stamenkovic, B.B. Blizanac, T. Tomoyuki, P.N. Ross, et al., *J. Am. Chem. Soc.* 127 (2005) 6819–6829.
- [62] S. Mukerjee, R.C. Urian, *Electrochim. Acta* 47 (2002) 3219–3231.
- [63] G. Tremiliosi-Filho, E.R. Gonzalez, A.J. Motheo, E.M. Belgsir, J.-M. Léger, C. Lamy, *J. Electroanal. Chem.* 444 (1998) 31–39.
- [64] K. Kunitatsu, M.G. Samant, H. Seki, M.R. Philpott, *J. Electroanal. Chem. Interfacial Electrochem.* 243 (1988) 203–208.
- [65] R. Jinnouchi, T. Hatanaka, Y. Morimoto, M. Osawa, *Electrochim. Acta* 101 (2013) 254–261.
- [66] Y. Sawatari, J. Inukai, M. Ito, *J. Electron Spectrosc. Relat. Phenom.* 64–65 (1993) 515–522.
- [67] P.W. Faguy, N. Markovic, R.R. Adzic, C.A. Fierro, E.B. Yeager, *J. Electroanal. Chem. Interfacial Electrochem.* 289 (1990) 245–262.
- [68] T. Iwasita, F.C. Nart, *J. Electroanal. Chem. Interfacial Electrochem.* 295 (1990) 215–224.
- [69] K. Kunitatsu, M.G. Samant, H. Seki, *J. Electroanal. Chem. Interfacial Electrochem.* 258 (1989) 163–177.
- [70] T. Iwasita, F.C. Nart, *Prog. Surf. Sci.* 55 (1997) 271–340.
- [71] C. Lamy, S. Rousseau, E.M. Belgsir, C. Coutanceau, J.-M. Léger, *Electrochim. Acta* 49 (2004) 3901–3908.
- [72] J.-M. Léger, S. Rousseau, C. Coutanceau, F. Hahn, C. Lamy, *Electrochim. Acta* 50 (2005) 5118–5125.
- [73] G. García, N. Tsiouvaras, E. Pastor, M.A. Peña, J.L.G. Fierro, M.V. Martínez-Huerta, *Int. J. Hydrogen Energy* 37 (2012) 7131–7140.
- [74] D.S. Corrigan, E.K. Krauskopf, L.M. Rice, A. Wieckowski, M.J. Weaver, *J. Phys. Chem.* 92 (1988) 1596–1601.
- [75] K. Ito, H.J. Bernstein, *Can. J. Chem.* 34 (1956) 170–178.
- [76] J.C. Morris, *J. Chem. Phys.* 11 (1943) 230–235.
- [77] L. Castanheira, W.O. Silva, F.H.B. Lima, A. Crisci, L. Dubau, F. Maillard, *ACS Catal.* 5 (2015) 2184–2194.
- [78] U. Schmiemann, U. Müller, H. Baltruschat, *Electrochim. Acta* 40 (1995) 99–107.
- [79] S.C.S. Lai, S.E.F. Kleyn, V. Rosca, M.T.M. Koper, *J. Phys. Chem. C* 112 (2008) 19080–19087.
- [80] F. Cases, M. López-Atalaya, J.L. Vázquez, A. Aldaz, J. Clavilier, *J. Electroanal. Chem. Interfacial Electrochem.* 278 (1990) 433–440.
- [81] R. Ianniello, V.M. Schmidt, J.L. Rodríguez, E. Pastor, *J. Electroanal. Chem.* 471 (1999) 167–179.
- [82] N.R. de Tacconi, R.O. Lezna, B. Beden, F. Hahn, C. Lamy, *J. Electroanal. Chem.* 379 (1994) 329–337.
- [83] J. Willsau, J. Heitbaum, *J. Electroanal. Chem. Interfacial Electrochem.* 194 (1985) 27–35.
- [84] J. Willsau, J. Heitbaum, *Electrochim. Acta* 31 (1986) 943–948.
- [85] J. Silva-Chong, E. Méndez, J.L. Rodríguez, M.C. Arévalo, E. Pastor, *Electrochim. Acta* 47 (2002) 1441–1449.
- [86] H. Wang, Z. Jusys, R.J. Behm, *J. Power Sources* 154 (2006) 351–359.
- [87] F. Vigier, C. Coutanceau, F. Hahn, E.M. Belgsir, C. Lamy, *J. Electroanal. Chem.* 563 (2004) 81–89.